Rare Metal Materials and Engineering
Volume 55, Issue 4, April 2026
Available online at www.rmme.ac.cn

Science Press

Cite this article as: Wang Xinyu, Mi Guangbao, Chen Yisi, et al. Combustion Behavior and Microstructure of Ti-Al-Mo-Zr-Sn-W Alloy After Laser Ignition[J]. Rare Metal Materials and Engineering, 2026, 55(04): 856-868.
DOI: https://doi.org/10.12442/j.issn.1002-185X.20250204.

ARTICLE

Combustion Behavior and Microstructure of Ti-Al-Mo-Zr-Sn-W Alloy After Laser Ignition

Wang Xinyu[1], Mi Guangbao[1], Chen Yisi[1,2], Sun Ruochen[1], Qiu Yuehai[1,2], Tan Yong[1,2]

[1] Aviation Key Laboratory of Science and Technology on Advanced Titanium Alloys, AECC Beijing Institute of Aeronautical Materials, Beijing 100095, China; [2] National Center of Novel Materials for International Research, Tsinghua University, Beijing 100084, China

Abstract: The combustion behavior of Ti-Al-Mo-Zr-Sn-W alloy (TC25G) was studied in a high-temperature and high-speed air flow environment using the laser ignition method combined with ultra-high temperature infrared thermometer, scanning electron microscope, X-ray diffractometer, and transmission electron microscope. The burn-resistant performance of TC25G and TC11 alloys was compared. Meanwhile, the microstructural characteristics, crystal structure, and formation mechanism of the combustion products of TC25G alloy were analyzed in detail. The results show that the high-temperature and high-speed air flow promotes combustion within the air flow temperature range of 200–400 °C and the air flow velocity range of 0–100 m/s. The combustion path advances along the direction of the air flow. The combustion of TC25G alloy mainly relies on the diffusion of the oxygen and the expansion of the combustion area caused by the movement of the melt. Based on the microstructure and composition of combustion product, it can be divided into the combustion zone, the melting zone, and the heat affected zone. During combustion, the formation of microstructures is closely correlated with the behavior of alloying elements and their selective combination with O. The major oxidation products of Ti are TiO and TiO_2. The oxides formed by Mo and W hinder the movement of the melt during the combustion. Al and Zr tend to undergo internal oxidation. Al_2O_3 precipitates on the surface of ZrO_2, forming a protective oxide layer that inhibits the inward diffusion of O. Moreover, the element enrichment at the interface between the melting zone and the heat affected zone increases the melting point on the solid side, hindering the migration of the solid-liquid interface.

Key words: Ti-Al-Mo-Zr-Sn-W alloy; laser ignition; combustion microstructure; burn-resistant mechanism; titanium fire

1 Introduction

Titanium alloy, as an important material for aero-engines, is prone to titanium fire accidents. Titanium fire mainly occurs in the high-pressure compressor. It is a combustion phenomenon of titanium alloys caused by abnormal friction between the titanium alloy casing and blades, foreign object friction, and splashing of melt under high-temperature friction[1–5]. Once combustion occurs, it will cause huge economic losses and casualties. The prevention and control of titanium fire is a worldwide problem that has long troubled and restricted the extensive application of titanium alloys[6]. In recent years, researchers have conduct extensive studies on the combustion of titanium alloys. Friction ignition and laser ignition are commonly used methods to investigate the combustion behavior and mechanisms of titanium alloys[3,6–11].

The laser ignition method ignites titanium alloy rapidly through heat accumulation. It can precisely control the power of the laser beam, the spot size, and the irradiation time. This method can obtain accurate parameters for evaluating the combustion characteristics of titanium alloys, with high accuracy of test values. It has great potential for development and application value[3], and is one of the most advanced methods for studying titanium alloy combustion. At present, some scholars have used this method to study the combustion behavior and mechanisms of Ti-Al alloys and near-α Ti superalloys[3,7,12]. It has been found that the Ti-Al-O ternary phase formed during the combustion of Ti-Al alloys can enhance the stability of the Al_2O_3 protective layer by reducing the decomposition pressure of the Al_2O_3. During the ignition stage

Received date: April 22, 2025
Foundation item: China "Ye Qisun" Science Foundation Project of National Natural Science Foundation (U2141222); Innovation Fund (8F231527Z)
Corresponding author: Mi Guangbao, Ph. D., Professor, Aviation Key Laboratory of Science and Technology on Advanced Titanium Alloys, AECC Beijing Institute of Aeronautical Materials, Beijing 100095, P. R. China, Tel: 0086-10-62496627, E-mail: guangbao.mi@biam.ac.cn

of TA19 alloy, the pore defects caused by gaseous TiO lead to the failure of the TiO_2 layer on the alloy surface, resulting in intense combustion. Actually, the study of combustion microstructure is an important way to gain a deep understanding of the combustion mechanisms of titanium alloys. When titanium alloys of Ti-V-Cr system are combusted, V_2O_5 and Cr_2O_3 are formed, which increase the density of the oxide layer and hinder the diffusion of O[13–15]. The formation of V-based solid solution phase can reduce the migration rate of Ti, effectively slowing down the preferential reaction between Ti and O[8]. When Ti-Cu-Al system alloys are combusted, they react with O to form CuO and CuO_2. CuO and CuO_2 consume a certain amount of O, thereby inhibiting the reaction of O with the alloy matrix[13–14,16]. Currently, the Ti-Al-Mo-Zr-Sn system titanium alloys are mainly used in aero-engines[17–18]. The combustion rate of TC11 alloy is significantly affected by the enrichment and distribution of alloying elements near the interface between the melting zone and the matrix[19–20]. The oxides in the combustion products of TA15 alloy are mainly composed of Al_2O_3 and TiO_2[6]. The combustion mechanism of TA19 alloy involves the formation of an oxygen-rich solid solution[9]. Overall, it has been demonstrated that forming a protective barrier like the ones mentioned above is the key to achieve good burn-resistant performance. The main mechanism for suppressing combustion is to slow down the supply of O to the alloy matrix and the diffusion of Ti to the combustion area.

TC25G alloy is a titanium superalloy belonging to Ti-Al-Mo-Zr-Sn-W system and is a $\alpha+\beta$ bi-phase titanium alloy. Researchers have achieved better properties by adjusting the content of each element within this system and selectively adding other β-stabilizing elements and refractory elements[17–18,21]. The composition of TC25G alloy is characterized by relatively high levels of Mo and Zr, as well as the inclusion of the refractory element W. The elemental characteristics of TC25G alloy give it excellent oxidation resistance, thermal stability, and creep performance. Therefore, it has good high-temperature comprehensive performance[22]. This alloy is widely used in critical components of aero-engines, such as high-pressure compressor rotor disks and blades. However, it is susceptible to the titanium fire, and there have been rare reports on the combustion of this alloy. In addition, the alloying elements in this alloy are numerous, and the combustion mechanism is more complex. The investigation into the effects of alloying elements and combustion microstructures on the combustion mechanism of this alloy is not complete. Therefore, further research is necessary.

Consequently, this study focused on combustion behavior under high-temperature and high-speed air flow and combustion microstructure of TC25G alloy, and it compared the combustion differences between TC25G alloy and TC11 alloy. Moreover, it further investigated the effects of combustion microstructure and alloying elements on the combustion mechanism. This study aims to provide a deeper understanding of the combustion mechanism of Ti-Al-Mo-Zr-Sn-W system titanium alloys and to further promote the application of TC25G alloy. In addition, this research is of great significance for the compositional optimization of titanium superalloys and the development of titanium fire prevention and control technologies for titanium alloys.

2 Experiment

Experimental material was TC25G alloy, and its chemical composition is listed in Table 1. The original microstructure is shown in Fig.1. There is a certain number of primary α phases in β transition matrix. It is a typical bi-phase microstructure. The combustion test samples were acquired by wire cutting, milling, and grinding. The sizes of the samples were 70 mm× 30 mm×2 mm, and the sample surface was clean and bright.

In this experiment, the laser ignition experimental device[23] was employed to ignite the TC25G superalloy. It consists of gas supply system, laser system, detection system, and combustion chamber. The sample was fixed in the fixture of the combustion chamber. The power of the laser system was 400 W. The duration of laser irradiation was set at 5 s. The experiment was implemented under the following environmental conditions: (1) air flow temperature of 200 °C with air flow velocity of 94.3, 86.8, and 75.7 m/s; (2) air flow temperature of 300 °C with air flow velocity of 94.3, 75.5, and 67.9 m/s; (3) air flow temperature of 400 °C with air flow velocity of 67.9, 60.4, 52.8, 45.3, 37.7, and 30.2 m/s. The pressure of the combustion chamber was 0.5 MPa. Moreover, experiments were conducted on TC11 and TC25G alloys at an air flow temperature of 450 °C and an air flow velocity of 150 m/s with different laser powers. After the equipment had been debugged, the laser system started and the sample was ignited. The combustion process was monitored in real-time using a high-speed infrared camera. After the sample had finished combustion, the experimental apparatus was shut down to obtain the combustion sample. During the experiment, the air flow velocity and temperature were kept constant. The directions of laser irradiation and air flow are shown in Fig.2, in which the orange area represents the laser irradiation spot.

Table 1 Chemical composition of TC25G alloy (wt%)

Al	Mo	Zr	Sn	W	Si	Ti
6.1	4.2	4.0	1.5	0.8	0.3	Bal.

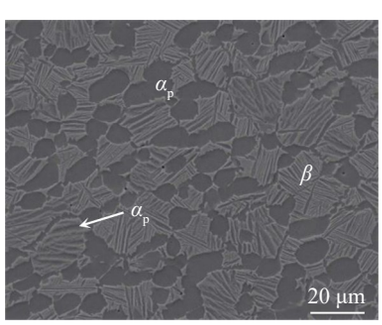

Fig.1 Original microstructure of TC25G alloy matrix

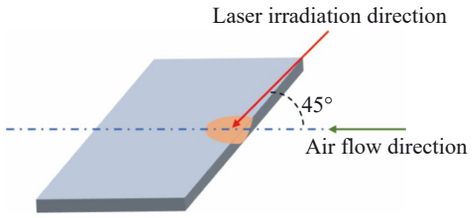

Fig.2 Schematic diagram of laser irradiation and air flow directions

The samples under the conditions of an air flow temperature of 200 °C and an air flow velocity of 75.5 m/s were selected for the analysis of combustion products. Wire cutting was used to obtain the sample from the combustion sample. The schematic diagram of the sampling and the analysis area is shown in Fig. 3. X-ray diffractometer (XRD, EVASTAR E3) was used to analyze the combustion products with a scanning angle of 10° to 90° and a scanning speed of 5°/min. Scanning electron microscope (SEM, TESCAN) and transmission electron microscope (TEM) were employed to observe the combustion microstructure. The elemental composition and distribution of combustion microstructure were investigated using an energy dispersive spectrometer (EDS), and thus the combustion mechanism was revealed.

3 Results and Discussion

3.1 Combustion behavior of TC25G alloy

The combustion of titanium alloys is accompanied by a series of oxidation reactions. Combustion process involves the transfer of oxygen and the diffusion of elements within the alloys. The composition of the alloys has a significant impact on the combustion behavior and mechanism. Moreover, the environment is also an important factor that cannot be ignored. Combustion tests were conducted on TC25G alloy under different air flow conditions. After the combustion is completed, one situation is that the sample is not burned through. For example, the macro-morphology of sample under a combustion condition of an air flow temperature of 400 °C and an air flow velocity of 30.2 m/s is shown in Fig. 4a. The other situation is that the sample is burned through, which is apparently a more severe combustion result. For example, the macro-morphology of sample under a combustion condition of an air flow temperature of 400 °C and an air flow velocity of 60.4 m/s is shown in Fig.4b. It can be observed that the combustion surface is rough, with resolidified combustion products hanging below. The

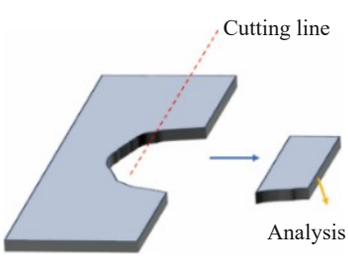

Fig.3 Schematic diagram of sampling and analysis area

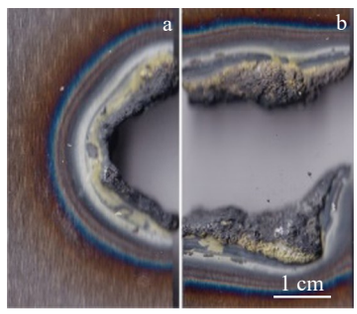

Fig.4 Macro-morphologies of TC25G alloy samples after laser ignition at 400 °C under different air flow velocities: (a) 30.2 m/s; (b) 60.4 m/s

combustion products are mainly ash-black and yellow, with granular oxides on the outermost layer. The surface of combustion samples has various colors, which are related to the phase composition and the light interference caused by oxide layers of different thicknesses[9]. Table 2 shows the burn-through states of combustion samples under different experimental conditions.

To further explore the combustion behavior of TC25G alloy in high-temperature and high-speed air flow, in situ observation of the combustion process was conducted. During the intense combustion of titanium alloys, substantial sparks and intense light are generated, which hinders optical image acquisition[3]. Consequently, a high-speed infrared camera was employed to display the combustion process. When the air flow temperature is 200 °C, the combustion processes at different air flow velocities are shown in Fig. 5. The dotted lines represent the edge of the sample. At the moment of laser irradiation (0–0.5 s), the temperature rises rapidly. After 1 s, the temperature can reach a peak of approximately 1880 °C, which is close to the melting point of TC25G alloy. After 3 s, high-temperature melt moving along the air flow and enveloping the alloy matrix is clearly observed. The combustion path advances along the direction of the air flow.

Table 2 Burn-through states of combustion samples under different air flow conditions

Number	Temperature/°C	Velocity/m·s^{-1}	Burn-through state
1	200	94.3	Yes
2	200	86.8	Yes
3	200	75.5	No
4	300	94.3	Yes
5	300	75.5	Yes
6	300	67.9	No
7	400	67.9	Yes
8	400	60.4	Yes
9	400	52.8	Yes
10	400	45.3	Yes
11	400	37.7	Yes
12	400	30.2	No

The high-temperature melt facilitates heat transfer, while the air flow supplies O and exerts a propelling force. Their combined effect leads to the expansion of combustion area, which rapidly spreads along the air flow direction and slowly to the surroundings. Comparing the combustion processes at 200 °C with different air flow velocities, it is distinctly observed that the increase in air flow velocity results in a longer movement distance of the melt and a greater propagation distance of combustion after 3 s. At 11 s, when air flow velocity is 75.5 m/s, the melt stops moving, and the combustion front starts to cool and gradually extinguishes. The reason is that the air flow is insufficient to drive the melt to continue moving. At this point, the cooling effect brought by the air flow dominates. At condition of 86.8 m/s, combustion continues with the flame spreading to the sample boundary. At condition of 94.3 m/s, the sample is even more severely damaged. The combustion process is observed with different air flow velocities at air flow temperatures of 300 and 400 °C using the same method. Through the high-speed infrared camera, it can be observed that when TC25G alloy can undergo relatively stable combustion without external energy input, the peak combustion temperature fluctuates between approximately 1600 and 2000 °C. In addition, to further investigate the effect of air flow velocity on the combustion process at different temperatures, the average combustion rate is defined as Eq. (1).

$$\bar{v} = L/t \quad (1)$$

where $\bar{v}$ is average combustion rate; L is the distance from the

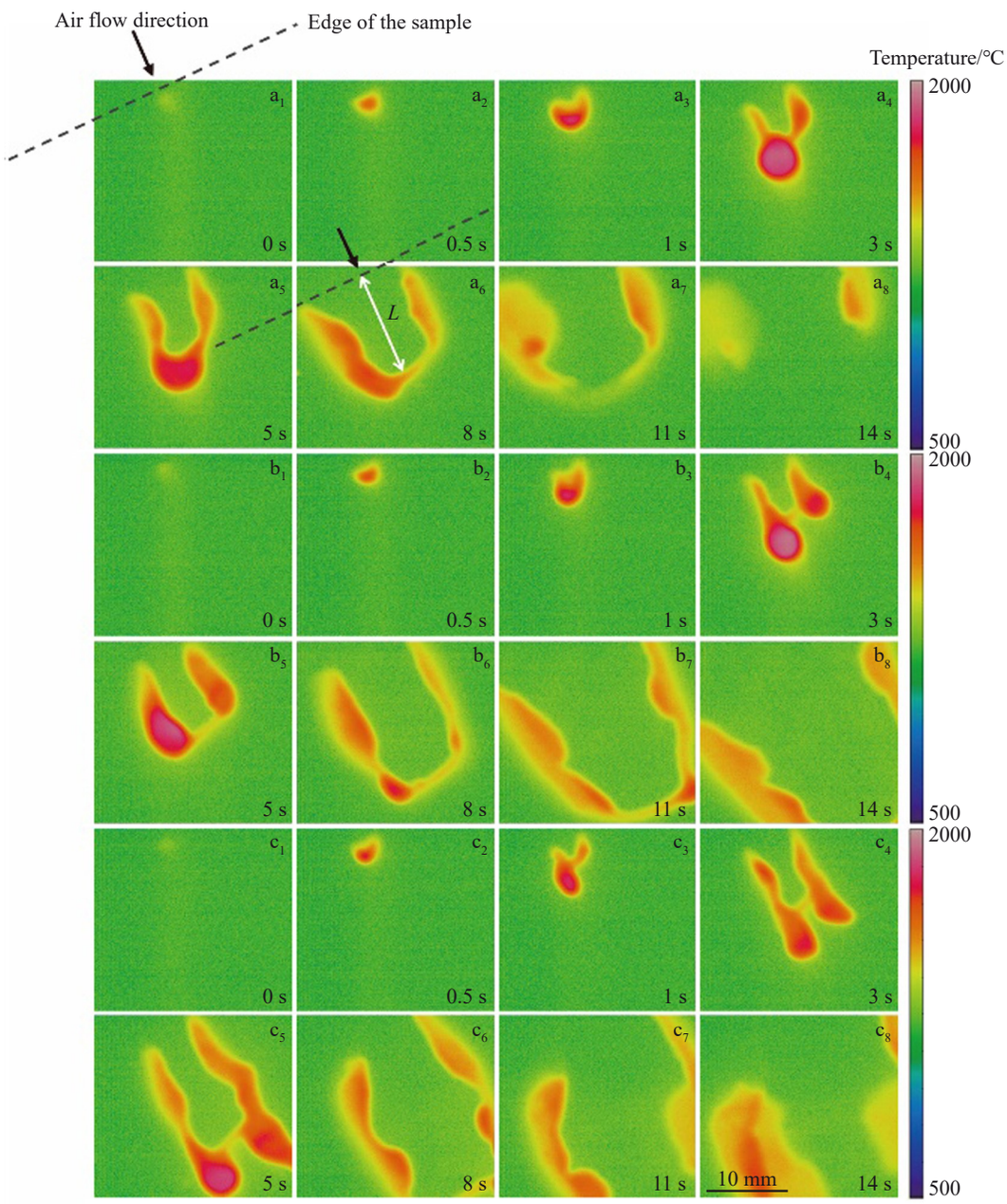

Fig.5 Combustion processes of TC25G alloy captured by a high-speed infrared camera at an air flow temperature of 200 °C under different air flow velocities: (a_1–a_8) 75.5 m/s, (b_1–b_8) 86.8 m/s, and (c_1–c_8) 94.3 m/s

laser spot position parallel to the air flow direction to the combustion area, as shown in Fig. 5a$_6$; t is the time after the laser is activated. The parameters L and $\bar{v}$ can directly reflect the degree of sample damage and the spread rate of combustion under the air flow environment, respectively. The relationship between the combustion time and the combustion length is shown in Fig. 6. It can be observed that, as combustion progresses, there is a distinct trend of attenuation in the slope. This indicates that the instantaneous combustion rate is decreasing. Taking the combustion duration of 10 s as the benchmark, the average combustion rate is calculated. At 200 °C, with air flow velocities of 94.3, 86.8, and 75.5 m/s, the average combustion rates are 2.8, 2.0, and 1.4 mm/s, respectively. It can be observed that when the air flow velocity increases from 75.5 m/s to 94.3 m/s, the average combustion rate is doubled. At 300 °C, with air flow velocities of 94.3, 75.5, and 67.9 m/s, the average combustion rates are 3.0, 2.3, and 1.5 mm/s, respectively. At 400 °C, with air flow velocities of 60.4, 45.3, and 30.2 s, the average combustion rates are 1.5, 1.1, and 0.7 mm/s, respectively. Results show that under the conditions of 200 – 400 °C and 0 – 100 m/s, the average combustion rate increases with the increase in air flow velocity, leading to more severe damage. In addition, it can be observed that when the air flow velocity is kept at 75.5 m/s, an increase in air flow temperature from 200 °C to 300 °C leads to an increase in both average combustion rate and combustion distance. The air flow temperature is an important factor that cannot be ignored in the combustion process. Based on Table 2, using combustion damage results as a standard, combustion experiment results at air flow temperatures of 200, 300, and 400 °C were compared to analyze the effect of air flow temperature on combustion behavior. The following boundary conditions cause the burn-through phenomenon of the samples: an air flow velocity of 86.8 m/s at 200 °C, 75.5 m/s at 300 °C, and 37.7 m/s at 400 °C. As the temperature increases, the sample can be burned through under a smaller air flow velocity. According to the above analysis, air flow is the driving force for combustion. In other words, with the increase in temperature, the driving force required to burn through the sample becomes smaller. Thus, the high-temperature environment is conducive to combustion.

Through the combustion experiments of TC25G alloy, the combustion behavior of titanium alloy is obtained under high-temperature air flow. Then, the combustion experiments are conducted on TC25G and TC11 alloys under air flow conditions close to their service temperatures. They both belong to the Ti-Al-Mo-Zr-Sn-W system titanium alloys. Compared with TC11 alloy, TC25G alloy has a higher content of refractory elements. Moreover, they both belong to the α+β titanium alloy, and Zr content in TC25G alloy is more than twice that of TC11 alloy. Fig. 7 shows the results of these titanium alloys after the combustion. It can be observed that at an air flow temperature of 450 °C and an air flow velocity of 150 m/s, only a very small area of TC11 alloy undergoes combustion under laser irradiation of 240 W, and signs of melt movement can be clearly seen. Under laser irradiation of 260 W, the sample is burned through. However, under the same laser irradiation, TC25G alloy only experiences combustion in a small area. When the laser power is increased to 275 W, the sample is burned through. The combustion areas of the samples in Fig. 7a$_1$ and 7b$_1$ were calculated. The combustion area of TC11 alloy is about 552 mm^2, and that of TC25G alloy is about 412 mm^2. Under higher energy input, TC25G alloy has less combustion damage. This indicates that under the same external energy input, TC25G alloy has better burn-resistant performance under the environment of high-temperature and high-speed air flow. Moreover, it can be observed that, compared with that of TC11 alloy, the combustion damage of TC25G alloy in the direction normal to the airflow is also less severe.

3.2 Combustion products of TC25G alloy

3.2.1 Major oxide composition of combustion products

XRD pattern of the combustion products of TC25G alloy is shown in Fig. 8. It demonstrates the major oxide composition, which includes TiO_2 and TiO. The chemical reactions that occur during the combustion of TC25G alloy are represented as Eq. (2) and Eq.(3).

$$2Ti + O_2 = 2TiO \quad (2)$$

$$2TiO + O_2 = 2TiO_2 \quad (3)$$

In the TC25G alloy, the high activity of Ti, coupled with the relatively low Gibbs free energy of TiO formation[24], results in the preferential formation of TiO. TiO is a low-valent metastable oxide that can be easily further oxidized. The O

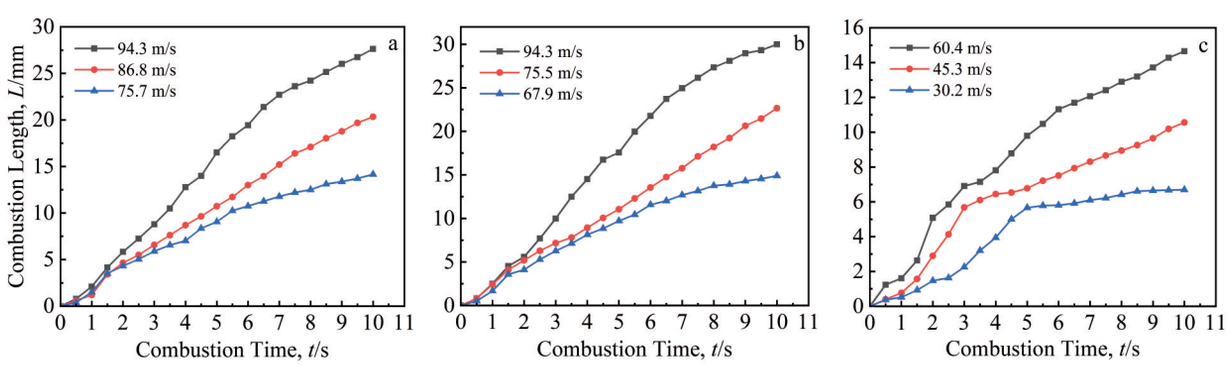

Fig.6 Relationship between combustion time and combustion length under different air flow velocities and temperatures: (a) 200 °C, (b) 300 °C, and (c) 400 °C

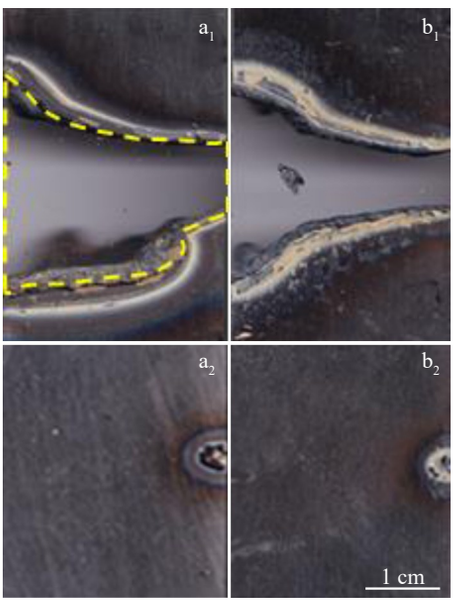

Fig.7 Combustion results of TC11 (a_1–a_2) and TC25G (b_1–b_2) alloys at an air flow temperature of 450 °C and an airflow velocity of 150 m/s with different laser powers: (a_1, b_2) 260 W; (a_2) 240 W; (b_1) 275 W

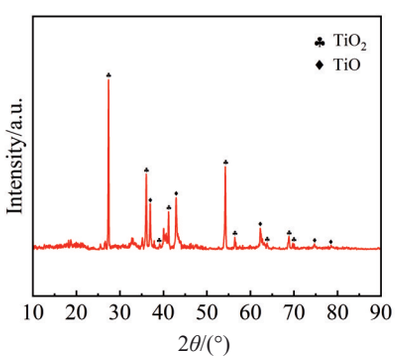

Fig.8 XRD pattern of combustion products of TC25G alloy

content at the combustion surface is sufficient to further oxidize TiO to TiO_2. When TC25G alloy is combusted, O diffuses into the alloy, creating an oxygen concentration gradient that decreases from the combustion surface to the alloy matrix. The internal oxygen content is not sufficient to oxidize TiO to TiO_2. This inference is consistent with the results of XRD analysis. In addition, according to XRD analysis, TiO_2 content is about 87.3wt% and TiO content is about 12.7wt%.

3.2.2 Microstructure and elemental composition of combustion products

Fig. 9 shows SEM image of the combustion microstructure. Based on the microstructure and composition of the combustion products of TC25G alloy, the combustion microstructure is divided into the combustion zone, melting zone, and heat affected zone. Moreover, according to the distribution of oxides, the combustion zone is further divided into the outer and inner sides.

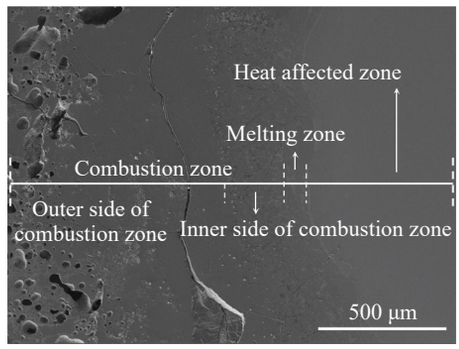

Fig.9 SEM image of combustion microstructure

The microstructure features and elemental composition vary in different zones. They are determined by the elemental diffusion during the combustion process, as well as the oxygen and temperature gradients. The combustion zone contains many defects. The inner side of the combustion zone is filled with numerous pores. The formation of these pores is attributed to the high cooling rate, which hinders gas escape from the melt. Additionally, in a high-speed air flow environment, gas is more likely to be entrained into the solidified structure. Numerous cracks are distributed in the combustion and melting zones, mainly caused by thermal stress and liquid phase volume contraction during solidification. The combustion zone is composed mainly of oxides. The melting zone consists of various oxygen-rich solid solution phase, and this zone exhibits typical solidification structures. The heat affected zone, influenced by temperature, has a structure that differs from the original structure, showing an interwoven structure of netlike β phase and lamellar α phase. It can also be observed that there is a clear interface between the melting zone and the heat affected zone. The microstructures of combustion zone are shown in Fig. 10a – 10d, and the EDS analysis is presented in Table 3. The microstructure of the melting zone is shown in Fig. 10e, with EDS analysis results in Table 4. The microstructure of the heat affected zone is shown in Fig. 10f, and corresponding EDS analysis is listed in Table 5.

The outer side of the combustion zone is mainly composed of gray phases (P1, P2), discontinuous black netlike phases (P3, P4), and white phases (P5, P6) distributed around the pores. Based on the EDS analysis results, combined with the XRD analysis, the gray phase is identified as TiO_2, while the discontinuous black netlike phase is composed of TiO_2 and Al_2O_3. Due to the low content of Al, a complete and dense Al_2O_3 film cannot be formed in the combustion microstructure[25]. The thickness of the netlike phase ranges between 0.2 – 1.0 μm. The white phase contains higher amounts of Mo and W, and is mainly composed of TiO_2 and the oxides of Mo and W, which are distributed extensively around the pores. During the combustion, the combustion peak temperature is about 2000 °C, reaching the boiling points of some oxides of Mo and W. Therefore, the oxides of Mo and W appear as the gaseous form mixed with the air in the

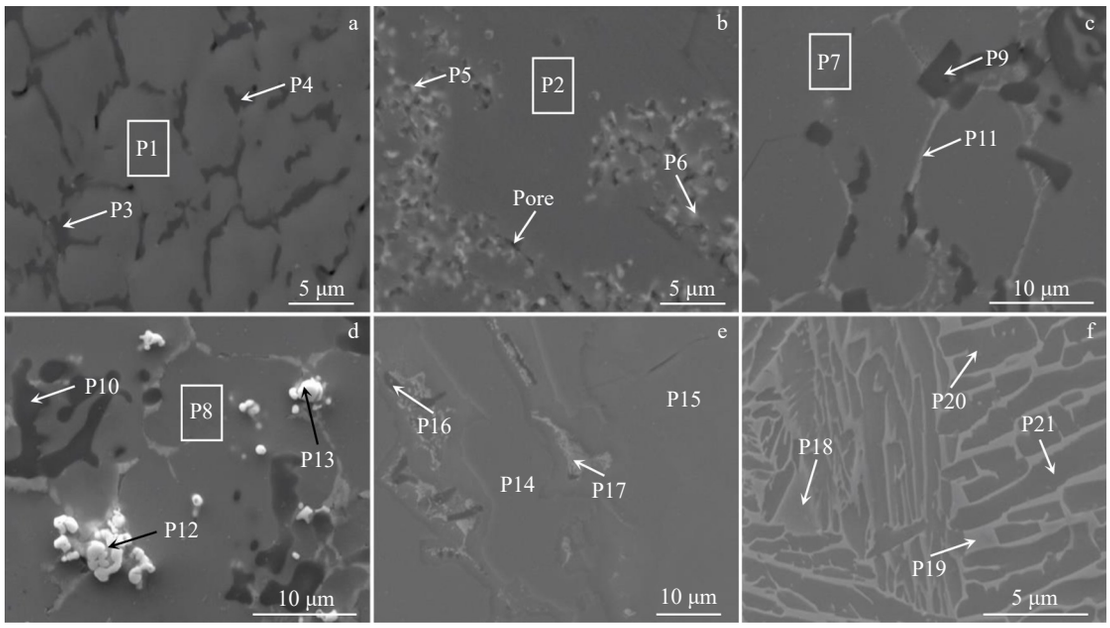

Fig.10 Typical microstructures of the outer side (a–b) and inner side (c–d) of combustion zone, melting zone (e), and heat affected zone (f) of TC25G alloy after combustion

Table 3 EDS analysis results of positions P1–P13 marked in Fig.10a–10d (at%)

Position	Ti	Al	Mo	Zr	W	O
P1	34.1	0.7	2.1	0.3	0.4	62.4
P2	33.8	2.7	0.4	0.4	0.2	62.5
P3	21.8	15.6	0.3	0.4	0.1	61.3
P4	25.0	13.9	0.5	0.4	0.1	60.1
P5	17.9	2.0	13.1	0.2	1.5	65.3
P6	19.9	1.8	10.8	0.4	1.5	65.6
P7	49.4	1.7	-	0.3	-	48.6
P8	48.4	2.1	0.1	0.3	-	49.1
P9	7.7	29.4	-	-	-	62.9
P10	5.3	34.3	-	-	-	60.4
P11	38.9	1.6	-	5.2	-	54.3
P12	27.6	3.0	39.3	0.2	6.3	20.8
P13	26.7	4.8	33.3	0.9	10.5	22.9

atmosphere. In the subsequent rapid cooling process, the gaseous oxides and air mixture cannot fully escape from the melt pool, thus forming pores. After cooling, these oxides solidify and are distributed around the pores.

The inner side of the combustion zone is mainly composed of gray phases (P7, P8), black blocky phases (P9, P10), white stripe phases (P11), and white granular phases (P12, P13). The atomic ratio of Ti to O in the gray phase is 1∶1. Combined with the XRD analysis, this phase is identified as TiO. The white stripe phase has a high content of Zr and is mainly

Table 4 EDS analysis results of positions P14 – P17 marked in Fig.10e (at%)

Position	Ti	Al	Mo	Zr	W	O
P14	60.7	0.7	0.1	0.3	0	38
P15	66.5	4.9	0.5	0.5	0.1	27.2
P16	9.7	29.9	0.5	0.3	0.1	59.4
P17	38.5	15.2	5.3	6.1	0.6	29.9

Table 5 EDS analysis results of positions P18 – P21 marked in Fig.10f (at%)

Position	Ti	Al	Mo	Zr	W	O
P18	64.2	16.2	3.7	2.4	0.5	11.6
P19	64.2	15.9	4.0	1.6	0.7	12.7
P20	65.8	11.9	1.9	1.1	0.5	18.1
P21	67.0	11.3	1.8	1.1	0.5	17.5

composed of TiO and ZrO_2. The black blocky phase is composed of TiO and Al_2O_3. Compared with the discontinuous black netlike phase on the outer side of the combustion zone, this phase has a larger area, a higher Al content, and a higher proportion in this zone. The white granular phase is sparsely distributed on the inner side of the combustion zone, with a protruding morphology and extremely high contents of Mo and W. This is similar to the defects produced during the metal smelting process. Under the action of high energy laser, the titanium alloy is heated and rapidly oxidized, releasing a large amount of heat, which promotes the combustion and melting of the alloy matrix. As the combustion area expands, in-situ combustion products and melt mixtures gradually cool down. The melting points of Mo and W in the melt pool are high, and their relative degree of supercooling is higher than that of titanium and other alloying elements. Under insufficient diffusion and convection, local segregation of Mo and W occurs. Furthermore, the peak temperature of the combustion is about 2000 °C, and all alloying elements have a strong tendency to undergo intense oxidation. Therefore, this phase is an oxide rich in Mo, W, and O. The oxides induced by faster cooling and solidification are entrained into the combustion melt, which helps to increase the viscosity of the melt and inhibit the migration of the melt.

In the melting zone, there is an irregular blocky precipitate phase, which shows a typical high-temperature solidification structure. This zone is mainly composed of gray blocky phases (P14), gray phases (P15), black phases (P16), and white phases (P17). The gray phase is the β-Ti. The gray blocky phase is the equiaxed α phase precipitated from the β phase during solidification, with an oxygen content of about 38at% . According to the Ti-O phase diagram, the maximum solubility of oxygen in titanium alloy is 33at%. Therefore, it is an oxygen-rich α-Ti solid solution phase. The solubility of oxygen in α-Ti is very high, and its oxygen content is significantly higher than that in the β-Ti solid solution phase. By consuming oxygen through the oxygen-dissolving capacity of α-Ti, the inward diffusion of oxygen is prevented. The β phase contains relatively higher amounts of Al and Mo. The white phase and the black phase are sparsely distributed in the melting zone with low content. The black phase has a higher content of Al. The white phase has relatively higher contents of Mo and Zr. According to previous research of our team, these two phases are mainly Ti-, Al-, Mo-, and Zr-based solid solution phases[6–9].

During the combustion, the temperature in the heat affected zone does not reach the melting point and remains near the β phase region. The high temperature is maintained for a short period, and the cooling rate is high. Residual β phase (P18, P19) exists between the lamellar α phases (P20, P21). In α+β type titanium alloy, this residual β phase forms a continuous netlike thin layer between the α lamellae. As shown in Fig. 10f, the interwoven structure of the netlike β phase and the lamellar α phase can be clearly observed. The α phase has a higher O content and lower Mo and Al contents compared to the β phase. It is consistent with the results in the melting zone. Studies have shown that the diffusion of Ti atoms from the heat affected zone to the melting zone is hindered by the Ti-based solid solution phase rich in Al and Mo[14,26].

3.2.3 Distribution characteristic and formation mechanism of elements in combustion microstructure

EDS element line scanning was performed over a range of approximately 1700 μm from the combustion zone to the heat affected zone, as shown in Fig. 11. The combustion zone is approximately located between 0 and 1000 μm, the melting zone is located between 1000 and 1100 μm, and the heat affected zone is located between 1100 and 1700 μm.

On the outer side of the combustion zone, the content of various elements fluctuates significantly. The reason is that the elements undergo intense oxidation at high temperatures, resulting in the presence of various oxides in this zone. Additionally, in the range of 0–350 μm, the content of Mo and W is much higher than that in other zones. During combustion, a large number of gaseous oxides of Mo and W are generated. These gaseous oxides mix with air to form numerous pores on the outer side of the combustion zone, as shown in Fig. 9. This leads to the accumulation of oxides of Mo and W. After cooling, these oxides revert to a solid state. As a result, the content of Mo and W is very high in this zone. It can also be observed that the formation of oxides leads to a decrease in titanium content in the combustion zone. The overall trend of titanium content from the combustion zone to the heat affected zone is increasing.

On the inner side of combustion zone and melting zone, the content of Al is relatively high. Al exhibits a tendency to diffuse inward. The reason for this phenomenon is related to the content of Ti and Al. In TC25G alloy, the low Al content tends to cause internal oxidation, forming Al_2O_3 at the interface between the oxide layer and the alloy matrix[7]. At the same time, this is also related to atomic embedment energy. The atomic embedment energy of Al atoms on the titanium surface is 5.63 eV, which is higher than that in the titanium matrix (5.26 eV)[6]. As shown in Fig. 10c and 10d, Section 3.2.2 mentions that the area, proportion, and Al content of the

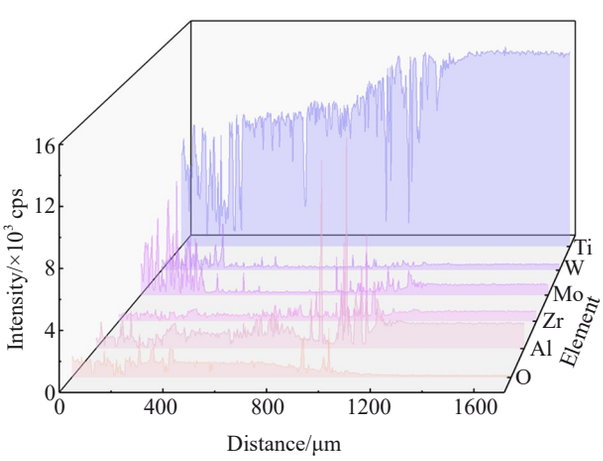

Fig.11 EDS element line scanning results from the combustion zone to the heat affected zone

blocky phase containing Al_2O_3 on the inner side of the combustion zone are much higher than those of the netlike phase on the outer side, which is also a manifestation of the tendency of Al to undergo internal oxidation. The inner side of combustion zone also contains TiO and ZrO_2. EDS element line scanning analysis shows that the Zr content increases from the combustion zone to the heat affected zone. Both Zr and Al tend to undergo internal oxidation. In this zone, the black blocky phase containing Al_2O_3 is largely attached to the netlike phase containing ZrO_2. TEM bright field image of this zone and the calibration diagrams of selected area electron diffraction (SAED) patterns are shown in Fig. 12. In Fig. 12a, at position I, cubic [010] TiO with a space group of $Fm\bar{3}m$ is formed. At position II, trigonal $[02\bar{1}]$ Al_2O_3 with a space group of $R\bar{3}c$ is formed. At the adjacent position III, monoclinic $[\bar{1}\bar{7}5]$ ZrO_2 with a space group of $P2_1/a$ is formed. This further confirms the existence of Al_2O_3 and ZrO_2 and clarifies their crystal structures in the combustion products. Studies have shown that ZrO_2 can act as a heterogeneous nucleation site for Al_2O_3[27]. Based on the analysis of the combustion behavior described above, the movement of the melt drives the continuous combustion, which is a dynamic process accompanied by oxidation, melting, and solidification, with the continuous formation of ZrO_2 and Al_2O_3. As the melt moves, Al_2O_3 precipitates during the solidification process, tending to nucleate and grow on the already formed ZrO_2 as a heterogeneous nucleation site, ultimately presenting a microstructure where Al_2O_3 is attached to ZrO_2. The role of the dense Al_2O_3 oxide layer in blocking oxygen transport has been confirmed by numerous studies. Meanwhile, the ZrO_2 oxide layer has also been widely used in preventing the diffusion of oxygen[28–30]. The netlike phase containing ZrO_2 compensates for the discontinuity of the Al_2O_3 phase. The line scanning result of the O content shows a distinct downward trend in the range from 700 μm to 1000 μm. The oxide layer microstructure of Al_2O_3 attached to ZrO_2 is highly effective in preventing the inward diffusion of the O.

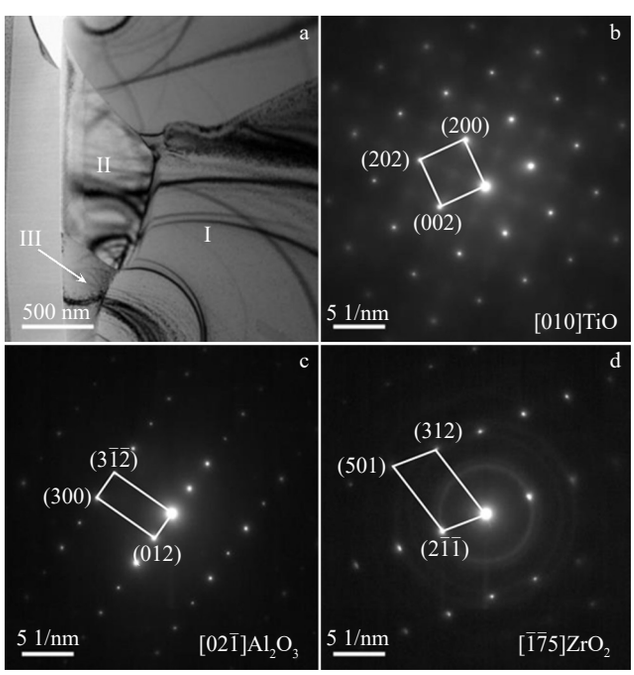

Fig.12 TEM bright field image of the inner side of combustion zone (a); SAED patterns of position I (b), position II (c), and position III (d) marked in Fig.12a

The distribution characteristics of Ti, Al, and Zr in the combustion zone are also the result of selective oxidation. From the perspective of thermodynamics, the Gibbs formation energy of Ti, Al, and Zr reacting with each mole of O_2 to form TiO, TiO_2, Al_2O_3, and ZrO_2 was calculated within the temperature range of 1600 – 2000 °C using the HSC Chemistry 6 thermodynamic analysis software. The results are shown in Fig. 13. Compared to TiO_2, TiO has a lower Gibbs formation energy, and TiO tends to form preferentially. This corroborates the inference in Section 3.2.1. In addition, it can be observed that the Gibbs formation energy of ZrO_2 is lower than that of Al_2O_3. This provides favorable thermodynamic conditions for the formation of ZrO_2, which facilitates the subsequent nucleation and growth of Al_2O_3. The reaction during combustion is also related to the diffusion of elements. From a kinetic perspective, since the combustion of TC25G alloy is driven by melt movement, it need to consider the diffusion of atoms in the melt. Generally, diffusion coefficients of atoms (D) in liquid metals or alloys can be solved by the Stocks-Einstein equation, as shown in Eq.(4).

$$D = kT/6\pi\eta r \tag{4}$$

where k is the Boltzmann constant (1.38×10^{-23} J·K^{-1}), η is the kinetic viscosity of the melts (Pa·s^{-1}), r is the radius of the diffusing atom (m), and T is the temperature (K). According to Hirai's model[31], the relation between viscosity and temperature of liquid alloys can be expressed, as shown in Eq. (5–7).

$$\eta = A\exp(B/RT) \tag{5}$$

$$A = \frac{1.7\times10^{-7}\rho^{2/3}T_m^{1/2}M^{-1/6}}{\exp(B/RT_m)} \tag{6}$$

$$B = 2.65T_m^{1.27} \tag{7}$$

where R is gas constant (8.314 J·mol^{-1}·K^{-1}); ρ is the density of alloy melt (kg·m^{-3}); T_m is the liquidus or melting temperature (K); M is the molar mass (kg·mol^{-1}). The material parameters required for Eq. (5–7) are shown in Table 6. By substituting the data in Table 6 into Eq. (5–7), Eq. (8–10) can be obtained.

$$\eta = 3.44\times10^{-4}\exp(4753/T) \tag{8}$$

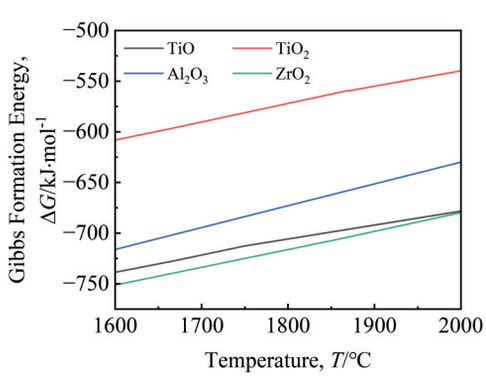

Fig.13 Gibbs formation energy of different oxides

Table 6 Material parameters required for Eq.(5–7)

Parameter	Value
ρ/kg·m^{-3}	4 080
T_m/K	1 933
M/kg·mol^{-1}	0.048 04
r(Al)/m	1.18×10^{-10}
r(Zr)/m	1.45×10^{-10}

$$D_{Al} = \frac{1.80 \times 10^{-11} T}{\exp(4753/T)} \quad (9)$$

$$D_{Zr} = \frac{1.47 \times 10^{-11} T}{\exp(4753/T)} \quad (10)$$

where D_{Al} and D_{Zr} are the diffusion coefficient of elements Al and Zr, respectively. The diffusion coefficient of Al is greater than that of Zr, and the content of Al in TC25G alloy is slightly higher than that of Zr. From a kinetic perspective, the diffusion rate of Al is higher. This corroborates that in the aforementioned elemental distribution analyses, the Zr content is relatively low on the outer side of the combustion zone, and the presence of the Al_2O_3 phase can be observed in the microstructure of the outer side of combustion zone in Fig. 10a, while ZrO_2 is virtually absent. Meanwhile, the tendency of Al_2O_3 to precipitate using ZrO_2 as a heterogeneous nucleation site also explains why the content of Al increases gradually towards the inner side of the combustion zone.

There are also certain fluctuations in the element content of the melting zone. It is caused by the formation of Ti-, Mo-, Zr-, and Al-based solid solution phases in this zone. The heat affected zone has a uniform distribution of elements overall. However, there is significant elemental fluctuation at the interface between the melting zone and the heat affected zone. It is related to the diffusion of elements near the interface. EDS element mappings are shown in Fig. 14. It can be observed that elemental enrichment occurs at the interface between the melting zone and the heat affected zone. During combustion, due to the high content and high activity of Ti, it is preferentially oxidized, resulting in intense diffusion from the solid side to the liquid side. It can be observed that Ti is enriched on the liquid side. Al, Mo, and Zr are enriched on the solid side. They exhibit an oxidation tendency. W and Sn, which have a lower proportion in TC25G alloy, are slightly enriched on the solid side. The elemental enrichment area is rich in high-melting-point elements, which can increase the melting point of the solid side. During combustion, there is no additional external energy input, and the increase in melting point of the solid side will result in more energy being consumed for the melting of the solid phase. Melting and solid-liquid interface migration are indirectly impeded. Moreover, the elemental enrichment area can effectively prevent the inward diffusion of O. EDS element mapping clearly shows a significant decrease in O content of the right side of the interface.

To further investigate the characteristics of elemental distribution and elemental content changes in different zones, the combustion microstructure was divided into several micro-areas, as shown in Fig.15. EDS analysis results of micro-areas are shown in Fig.16.

The variation trends of the element contents can be clearly observed, which are basically consistent with the conclusions drawn from line scanning analysis. Furthermore, the element contents of each micro-area can be determined. In the outer side of combustion zone, O content is 30wt%–40wt%. In the inner side of combustion zone, O content is 20wt%–30wt%. Then, under the influence of various protective barriers formed during the combustion, the diffusion of O is hindered. So, the O content drops sharply. In Fig.16, the oxygen content in the micro-area on the right side of the boundary between the melting zone and the heat affected zone is only about 2.4wt%. It can also be observed that in three micro-areas from 0 μm to 280 μm, there are numerous pores and the Mo and W oxides mentioned in the above analysis. In these micro-areas, the Mo content is between 4wt% and 10wt%, and the W content is between 2wt% and 6wt%, both of which are much

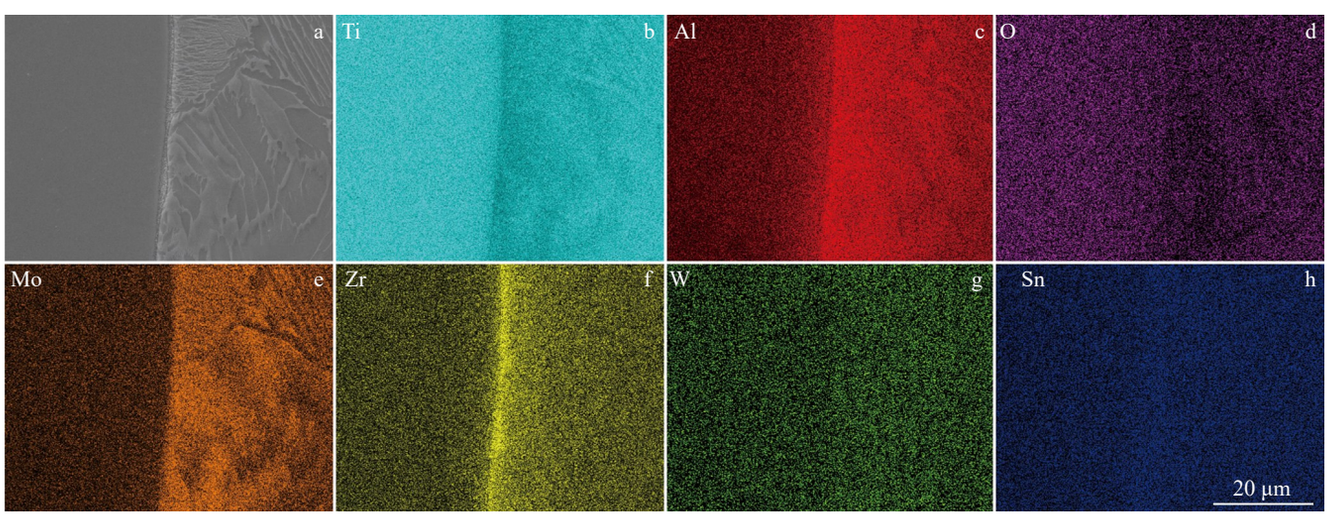

Fig.14 SEM image (a) and corresponding EDS element mappings (b–h) at the interface between the melting zone and the heat affected zone

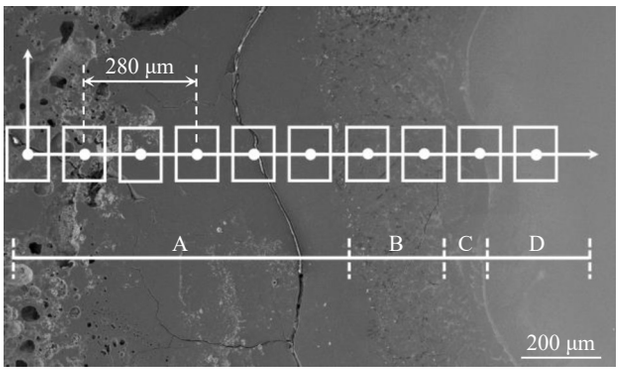

Fig.15 Schematic diagram of the division of micro-areas in the combustion microstructure (A represents outer side of combustion zone, B represents inner side of combustion zone, C represents melting zone, and D represents heat affected zone)

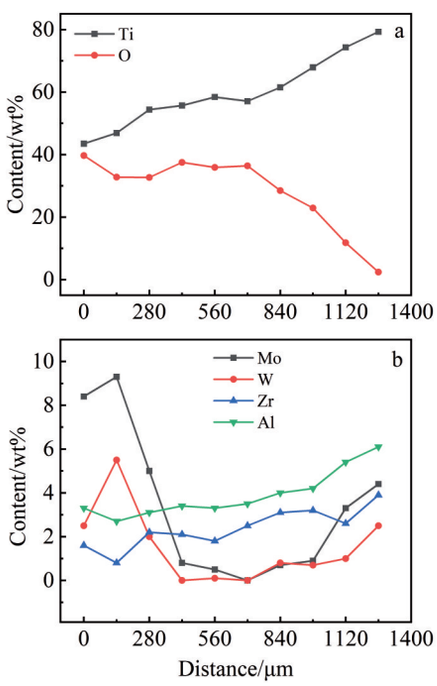

Fig.16 EDS analysis results of micro-area composition in combustion microstructure: (a) Ti and O; (b) Mo, W, Zr, and Al

higher than that in other areas. In the micro-areas between 840 – 980 μm containing microstructure of the Al_2O_3 attached to ZrO_2, the Al and Zr contents are slightly higher. Al content is about 4wt% and Zr content is about 3wt% in these areas.

Through the analysis of microstructure, distribution, and content of alloying elements, the formation mechanism of combustion microstructure can be basically revealed. Schematic diagram of combustion microstructure formation mechanism is shown in Fig. 17. The roles and mechanisms of various elements in titanium alloy combustion can be traced back via formation mechanism of combustion microstructure. From the above analysis, combustion relies mainly on oxygen diffusion and movement of melt. Therefore, blocking oxygen diffusion and movement of melt is the key way to prevent

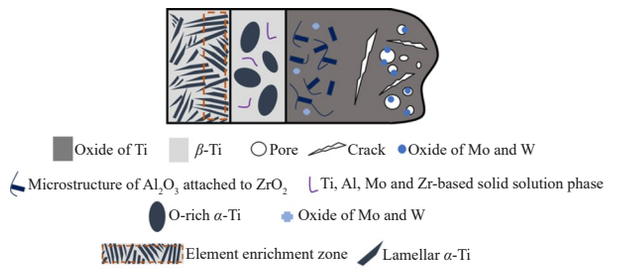

Fig.17 Schematic diagram of combustion microstructure formation mechanism

titanium fires from causing more severe material damage. Alloying elements significantly affect the combustion process and have potential burn-resistant mechanisms. It is the differences in the protective barriers formed during combustion that lead to the differences in the burn-resistant performance of TC25G and TC11 alloys. Based on the previous research of our team on the burn-resistant performance of TC11 alloy[20] in combination with studies of other researchers on the combustion microstructure of TC11 alloy[19,26], the similarities and differences in the microstructure and combustion mechanisms between TC25G and TC11 alloys were compared. It is found that TC25G alloy also contains a titanium-based solid solution phase rich in Al and Mo, with a large amount of dissolved O. However, in the combustion microstructure of TC11 alloy, Al_2O_3 and ZrO_2 are mostly distributed independently, with only a small amount of Al_2O_3 attached to the ZrO_2. Moreover, considering the elemental characteristics of TC25G alloy, the elemental behavior during combustion was further analyzed. Mo and W oxides are abundant on the combustion surface and distributed around the pores. This demonstrates that the volatilization phenomenon occurs after Mo and W form oxides. Vaporization carries away heat and enhances heat dissipation, indirectly hindering the movement of the melt. During the intense oxidation of Ti, Al and Zr take part in the oxidation process, and these two elements tend to undergo internal oxidation. During the continuous processes of melting and solidification, an oxide layer structure connected by Al_2O_3-ZrO_2 is formed. Due to the low Al content in TC25G alloy, Al_2O_3 cannot form a dense oxide film alone, which reduces its ability to hinder oxygen diffusion. However, the combined Al_2O_3-ZrO_2 oxide layer partially compensates for this deficiency and achieves a synergistic effect. On the one hand, Al_2O_3 is an excellent barrier against oxygen. Al_2O_3 has a variety of crystalline forms. Generally, it will be transformed into the thermodynamically stable α-Al_2O_3 at temperatures above 1200 °C[32]. The calibration results of SAED pattern in Fig. 12c also prove the existence of this phase. α-Al_2O_3 belongs to the trigonal crystal system, where oxygen ions form a hexagonal close-packed arrangement. This arrangement leads to a high packing density of oxygen ions, resulting in a compact and stable crystal structure. Thus, it effectively hinders oxygen diffusion. On the other hand, ZrO_2 has low thermal conductivity. It can slow down heat transfer. The

Al_2O_3-ZrO_2 structure forms effective protective barrier during TC25G alloy combustion. In addition, the enrichment of high-melting-point elements slows down the movement of melt.

4 Conclusions

1) The combustion of TC25G alloy mainly relies on the O diffusion and the expansion of combustion area caused by the movement of melt driven by high-temperature and high-speed air flow. The combustion path advances along the direction of the air flow. The combustion area expands rapidly along the direction of the air flow and spreads slowly to the surroundings. The high-temperature and high-speed air flow promotes combustion within the air flow temperature range of 200–400 °C and the air flow velocity range of 0–100 m/s. The increase in air flow velocity leads to a higher average combustion rate and more severe combustion damage. Moreover, under the environment of high-temperature and high-speed air flow at 450 °C, TC25G alloy has better burn-resistant performance than TC11 alloy.

2) The composition of combustion microstructure is as follows: TiO_2, Al_2O_3, and oxides of Mo and W on the outer side of combustion zone; TiO, Al_2O_3, ZrO_2, and oxides of Mo and W on the inner side of combustion zone; Ti-, Al-, Mo-, and Zr-based solid solution phases in the melting zone; Ti-based solid solution phase in the heat affected zone.

3) The alloying elements Al, Zr, Mo, and W in TC25G alloy have an impact on the combustion mechanism. Mo and W combine with O to form oxides, which helps to impede the movement of the melt. Al and Zr are prone to internal oxidation. The oxide layer microstructure of Al_2O_3 attached to ZrO_2 significantly inhibits the inward diffusion of O. The O-rich α-Ti consumes O, further preventing the inward diffusion of O. Element enrichment occurs at the interface between the melting zone and the heat affected zone, effectively preventing the diffusion of O into the alloy matrix. In addition, the enrichment of Mo and W can increase the melting point of the solid phase side, effectively preventing the continuous migration of the solid-liquid interface.

References

1 Mi Guangbao, Sun Ruochen, Qiu Yuehai *et al*. *Journal of Materials Engineering*[J], 2025, 53(1): 143 (in Chinese)

2 Wu Mingyu, Mi Guangbao, Li Peijie *et al*. *Acta Physica Sinica*[J], 2023, 72(16): 166102 (in Chinese)

3 Sun R C, Mi G B. *Rare Metal Materials and Engineering*[J], 2024, 53(9): 2405

4 Ouyang P X, Mi G B, Li P J *et al*. *Materials*[J], 2018, 11(11): 2141

5 Wang C Z, Li Z B, Dou C H *et al*. *Combustion Science and Technology*[J], 2024, 196(15): 3359

6 Sui Nan, Mi Guangbao, Yan Mengqi *et al*. *Rare Metals*[J], 2018, 37(11): 952 (in Chinese)

7 Wu Mingyu, Mi Guangbao, Li Peijie *et al*. *Journal of Materials Engineering*[J], 2024, 52(5): 1 (in Chinese)

8 Mi Guangbao, Huang Xu, Cao Jingxia *et al*. *Acta Physica Sinica*[J], 2016, 65(5): 225 (in Chinese)

9 Sui Nan, Mi Guangbao, Cao Jingxia. *Rare Metal Materials and Engineering*[J], 2022, 51(9): 3263 (in Chinese)

10 Zhang C, Xing P, Li Z B *et al*. *Metals*[J], 2023, 13(6): 1020

11 Ouyang P X, Mi G B, Cao J X *et al*. *Materials Today Communications*[J], 2018, 16: 364

12 Wu Mingyu, Mi Guangbao, Li Peijie. *Acta Physica Sinica*[J], 2024, 73(8): 233 (in Chinese)

13 Chen Y N, Yang W Q, Bo A X *et al*. *Materials and Design*[J], 2018, 156: 588

14 Shao L, Li W S, Li D Y *et al*. *Journal of Alloys and Compounds*[J], 2023, 960: 170584

15 Mi G B, Huang X, Cao J X *et al*. *Transactions of Nonferrous Metals Society of China*[J], 2013, 23(8): 2270

16 Chen Y N, Huo Y Z, Song X D *et al*. *International Journal of Minerals, Metallurgy and Materials*[J], 2016, 23(2): 215

17 Liu Z M, Xin S W, Zhao Y Q *et al*. *Materials*[J], 2023, 16(12): 4462

18 Liu Z M, Xin S W, Zhao Y Q *et al*. *Metals*[J],2023, 13(12): 1975

19 Shao L, Xie G L, Liu X H *et al. Corrosion Science*[J], 2020, 168, 108564

20 Mi Guangbao, Cao Chunxiao, Huang Xu *et al*. *Journal of Aeronautical Materials*[J], 2014, 34(4): 83 (in Chinese)

21 Xin S W, Liu X H, Zhang S Y *et al. Rare Metal Materials and Engineering*[J], 2023, 52(11): 3981

22 Zhang Xiaoyuan, Liu Xianghong, Du Yuxuan *et al*. *Rare Metal Materials and Engineering*[J], 2023, 52(12): 4227 (in Chinese)

23 Mi Guangbao, Chen Hang. *Chinese Patent*[P], ZL201711188505.5, 2017 (in Chinese)

24 Liu Y D, Gu W S, Pei Z L *et al*. *Materials Letters*[J], 2023, 351: 135002

25 Lv W, Li X, Wei Z K *et al*. *Rare Metal Materials and Engineering*[J], 2023, 52(12): 4276

26 Shao L, Li Z B, Yu J B *et al*. *Corrosion Science*[J], 2021, 192: 109868

27 Li X, Bao Y P, Wang J *et al*. *Metallurgical Research & Technology*[J], 2024, 121(5): 514

28 Wu Liangliang, Yin Ruozhan, Chen Zhaoxu *et al*. *Journal of Chinese Society for Corrosion and Protection*[J], 2024, 44(6): 1423 (in Chinese)

29 Ge Wen, He Taisong, Wang Meijiao *et al*. *Coatings*[J], 2020, 10(4): 332

30 Coloma R R, van de Kruijs R W E, Sturm J M *et al*. *Journal of Applied Physics*[J], 2017, 121(11): 115303

31 Hirai M. *ISIJ International*[J], 1993, 33(2): 251

32 Wang J P, Ling Y H, Lu Z X *et al*. *Applied Surface Science*[J], 2020, 515: 146053

激光点火Ti-Al-Mo-Zr-Sn-W合金燃烧行为与组织

王新宇[1]，弭光宝[1]，陈义斯[1,2]，孙若晨[1]，邱越海[1,2]，谭　勇[1,2]
(1. 中国航发北京航空材料研究院 先进钛合金航空科技重点实验室，北京 100095)
(2. 清华大学 新材料国际研发中心，北京 100084)

摘　要：采用激光点火实验结合超高温红外测温以及SEM、XRD和TEM等分析方法，研究典型Ti-Al-Mo-Zr-Sn-W合金（TC25G）在高温高速气流环境下的燃烧行为，并与TC11钛合金的阻燃性能进行比较，进而分析燃烧产物组织特征、晶体结构及形成机理。结果表明：在气流温度为200~400 ℃，气流速度为0~100 m/s范围内，高温高速气流能够促进TC25G钛合金持续燃烧，燃烧路径朝气流方向推进；TC25G钛合金的燃烧主要依靠氧的扩散与熔体移动所导致的燃烧区域扩展。基于合金燃烧产物组织与成分特点可以将其划分为燃烧区、熔凝区、热影响区等不同区域，燃烧过程组织特征的形成与合金元素行为及其与氧的选择性结合密切相关。燃烧区Ti的主要氧化产物为TiO和TiO_2，燃烧过程中形成的Mo、W元素的氧化混合物阻碍了熔体的移动，Al和Zr倾向于发生内氧化，Al_2O_3在ZrO_2表面析出并形成了氧化层组织，构成了保护性屏障，抑制了O向内扩散。熔凝区与热影响区界面处的元素富集能够提高固相侧的熔点，阻碍固-液界面的迁移。

关键词：Ti-Al-Mo-Zr-Sn-W合金；激光点火；燃烧组织；阻燃机理；钛火

作者简介：王新宇，男，2001年生，硕士生，中国航发北京航空材料研究院先进钛合金航空科技重点实验室，北京 100095，电话：010-62496627，E-mail：15010615564@163.com